Mechanism and Machine Theory 203 (2024) 105810

Contents lists available at ScienceDirect

Mechanism and Machine Theory

journal homepage: www.elsevier.com/locate/mechmt

Research paper

Reducing backward motion of stick-slip piezoelectric actuators using dual driving feet designed by asymmetric stiffness principle[☆]

Jie Ling [a,*], Hongtao Peng [a], Yuzhou Duan [a], Micky Rakotondrabe [b]

[a] College of Mechanical and Electrical Engineering, Nanjing University of Aeronautics and Astronautics, Nanjing 210016, China
[b] University of Technologie Tarbes Occitanie Pyrénées, University of Toulouse alliance, Tarbes 65016, France

ARTICLE INFO

Keywords:
Asymmetric stiffness
Compliant mechanism
Piezoelectric actuator
Stick–slip motion

ABSTRACT

Stick–slip piezoelectric actuators (SSPEAs) have drawn attention for their features of simple structure and high positioning accuracy. However, the backward motion has always been a major problem that limits driving speed and smoothness. Existing methods mainly focus on control methods and driving signal optimization, while few efforts emphasize mechanical structure optimization. To address this problem from the root of structure design, a novel SSPEA based on the principle of asymmetric stiffness is developed. A dual-driving feet configuration generates phase differences between two feet when feeding sawtooth driving signals. The core idea is that the backward motion of one driving foot can be compensated by another foot making full use of the phase difference due to the asymmetric stiffness compliant mechanism (ASCM). Kinematic and static models are built and the structural dimensions are then determined. Finite element analysis is conducted preliminarily to test the output performance. A physical prototype is fabricated and experimentally verified. Experimental results show the proposed actuator with ASCM achieves smaller backward motion and larger step size ranging from 250 to 1400 Hz driving frequencies compared with traditional triangular compliant mechanism (TTCM). The maximum speed is obtained as 47.2 mm/s with a resolution of 0.07 μm.

1. Introduction

Piezoelectric actuator (PEA) is a kind of micro-actuator with considerable advantages in high resolution, fast response, anti-electromagnetic interference, etc [1–5]. These advantages make the PEAs ultra popular in high-precision fields including microscopy [6], flow control valve [7], micromanipulation [8], etc. As shown in Fig. 1(a), according to the employed vibration states, PEAs can be divided into two main categories: resonant PEAs [9] and non-resonant PEAs [10]. The resonant PEAs can be further classified into traveling wave PEAs [11], standing wave PEAs [12], and composite vibration modes PEAs [13]. Whereas the non-resonant PEAs contain direct drive type, inchworm drive type [14,15], inertial impact type [16], and stick–slip type [17–25]. Among these types of PEAs, stick–slip PEAs (SSPEAs) have some unique advantages of simple structure, high positioning accuracy, and low manufacturing and assembly requirements [10,26,27].

Fig. 1(b) concisely presents the driving principle of a typical SSPEA. Generally, it consists of a piezoelectric stack (PES), a connector (mostly a block or a compliant mechanism (CM)), and a mover. The mover is pushed forward due to the friction between

---

[☆] This work was supported by the Natural Science Foundation of Jiangsu Province, China (Grant No. BK20210294), and by the International Joint Laboratory of Sustainable Manufacturing, Ministry of Education, China and the Fundamental Research Funds for the Central Universities, China (Grant No. NG2024016).

[*] Corresponding author.
E-mail addresses: meejling@nuaa.edu.cn (J. Ling), SZ2205097@nuaa.edu.cn (H. Peng), dyz@nuaa.edu.cn (Y. Duan), mrakoton@uttop.fr (M. Rakotondrabe).

https://doi.org/10.1016/j.mechmachtheory.2024.105810
Received 24 June 2024; Received in revised form 3 September 2024; Accepted 8 October 2024

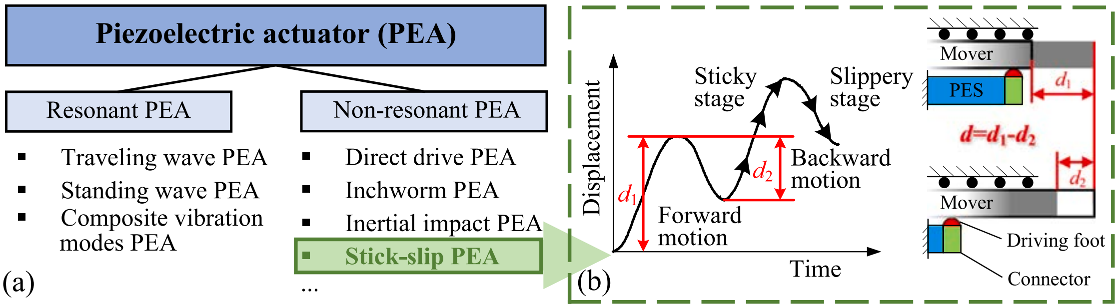

Fig. 1. The SSPEA. (a) The classification category and (b) the driving principle of the SSPEA. Abbreviation: SSPEA, stick–slip piezoelectric actuator; PES, piezoelectric stack.

the connector and the mover, and the friction part on the connector is figuratively called the *driving foot*. The mover produces one step $d = d_1 - d_2$ in one driving period through two stages, i.e., a sticky stage where the driving foot slowly moves the mover forward d_1 by feeding the PES a slow rise signal, and a slippery stage where the driving foot quickly moves back and makes the mover backward d_2 by feeding the PES a quick descent signal. Recently, researchers have proposed numerous SSPEAs with diverse configurations of which speed is one of the most important parameters [10,26].

To increase the output speed, based on the aforementioned stick–slip principle, some approaches are proposed. The first approach is to increase the driving frequency. This is not only related to the performance of the piezoelectric material but also to the structural mode of the actuator. In general, when the frequency reaches a certain threshold, the “stick” part starts to lose and the displacement d_1 is reduced. Thus, the stick–slip motion would deteriorate at higher frequencies [21].

The second approach is to reduce the backward motion d_2 to increase the total step size d. Based on this principle, many studies are carried out. The realization of backward motion suppression in these studies falls mainly between two methods: optimizing driving signals and collaborative compensation. For the first method, based on the method of ultrasonic friction reduction, Ning et al. [19] added high-frequency components to the driving signal (traditional sawtooth waves) when PES rapidly contracts. The experimental results showed that the actuator speed increased by 17%. Based on the principle of minimum friction work, Wang et al. [20] used a genetic algorithm to optimize the rising edge of serrated driving signals. For the second method, Qiu et al. [21] proposed a novel cooperative compensation method with two identical SSPEAs. When one PEA is performing a return motion, the other PEA is performing a forward motion to reduce backward stroke and increase speed. Results show that the maximum step length of the actuator at 250 Hz is 4.45 μm, 40% more than that of a traditional single stator. Tang et al. [22] proposed a new sequential control method to suppress the backward motions. Dong et al. [23] proposed a stick–slip linear PEA using an active-locking mechanism with two mechanisms. The maximum output speed and maximum output force of the prototype are 2.26 mm/s and 1.6 N under 100 V, respectively. Tian et al. [24] proposed an SSPEA with a passive damping driving foot to restrain the backward motion. The backward ratio is less than 1% when the foot has an appropriate clamping force. Liu et al. [25] proposed an SSPEA in a dual stator coordinated motion mode. Compared with the traditional single stator motion mode, the speed is increased to 1.04 rad/s, which is 40% faster than the traditional type. In [28], an inertial block produces different inertia by feeding asymmetric excitation signals so that the friction between the stator and the rotor is adjusted to achieve smooth motion. However, existing methods mainly focus on control methods or driving signal optimization to reduce the backward motion. These methods are not universal for different configurations of SSPEAs, and the increase in control degrees of freedom requires an increase in the number of PESs. Moreover, the performance is improved at the expense of increased complexity of the driving signal, where high requirements are posed for the control equipment.

To address this problem from the root of structure design, this paper proposes a new type of SSPEA with a dual-driving feet configuration based on the principle of asymmetric stiffness. There is a stiffness difference between the input and two output driving feet. Utilize the stiffness difference between the two driving feet to achieve the difference in response time, thereby achieving the goal of compensating for return travel. Hence, the output speed can be improved without adding any additional PES or driving signal optimization.

The remainder of this paper is organized as follows. Section 2 describes the configuration and working principle of the developed SSPEA. Then, the analytical model and finite element (FE) simulations of the actuator is performed in Section 3. For validation, experiments and analysis of its output performance under various working conditions are included in Section 4. Finally, the conclusions are made in Section 5.

2. Configuration and working principle

In this section, the proposed dual-driving feet SSPEA, which is designed based on the principle of asymmetric stiffness, is introduced. First, the configuration of the actuator and the detailed structure of the CM is introduced. Then, the working principle of the proposed actuator with backward motion compensation is described.

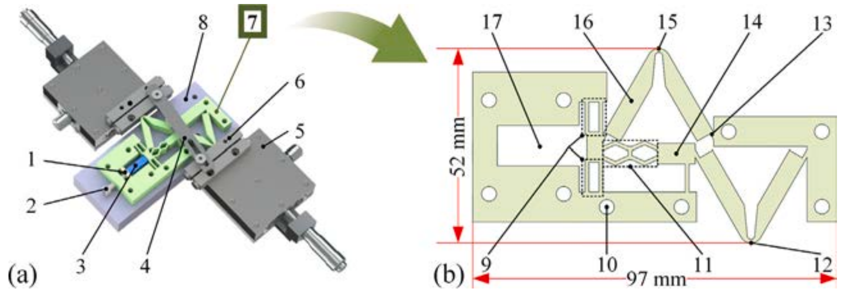

Fig. 2. The computer-aided design diagram of the proposed SSPEA platform: (a) the components of the platform: 1-Ceramic shim; 2-Pre-load bolt; 3-Piezoelectric stack (PES); 4-Connecting rod; 5-Micro-adjusting platform; 6-Slider; 7-Proposed asymmetric stiffness compliant mechanism (ASCM); 8-Supporting base, and (b) the detailed structure of the ASCM: 9-Flexure-guided hinge; 10-Fixing hole; 11-Cellular hinge; 12-Lower driving foot; 13-Rotational hinge; 14-Mass block; 15-Upper driving foot; 16-Rigid rod; 17-PES installation groove.

Table 1
Structural parameters of the asymmetric stiffness compliant mechanism.

Parameter	l_1	l_2	l_3	l_4	l_5
Value	27.44 mm	27.44 mm	27.44 mm	27.44 mm	24.74 mm
Parameter	l_6	Φ_1	Φ_2	Φ_3	Φ_4
Value	10.23 mm	240°	120°	120°	200.88°
Parameter	Φ_5	Φ_6	E	T	w_F
Value	180°	90°	209 GPa	8 mm	1 mm
Parameter	l_F	w_{fg}	l_{fg}	w_i $(i = \text{A, C, E, H})$	l_i $(i = \text{A, C, E, H})$
Value	7.53 mm	1 mm	8 mm	1 mm	1.63 mm
Parameter	w_i $(i = \text{B, G})$	l_i $(i = \text{B, G})$			
Value	1.69 mm	2.41 mm			

2.1. Configuration

The configuration of the proposed SSPEA platform is shown in Fig. 2(a), which consists of a ceramic shim, a pre-load bolt, a PES, a connecting rod, two micro-adjusting platforms, two sliders as the movers, the proposed asymmetric stiffness CM (ASCM), and the supporting base. The base and two micro-adjusting platforms are fixed to the optical platform with screws. The two micro-adjusting platforms each equipped with a set of linear guides are used to control the assembly pre-load between the two driving feet and the sliders. The PES is mounted by the pre-load bolt, serving as the power source for driving the base-mounted ASCM. The stick–slip motion of the ASCM drives the upper and lower sliders to move forward. The connecting rod is used to connect two sliders to ensure synchronous movement. The pre-load bolt is used to adjust the pre-load of the PES.

The detailed structure of the designed ASCM is presented in Fig. 2(b). The ASCM is a lumped flexible hinge CM, which means the compliant parts of the ASCM are lumped so that can be regarded as “flexure hinges”, and the other parts of the ASCM serve as rigid bodies. As shown in this subfigure, the flexure-guided hinge is directly pushed by the PES, which provides pre-load to the PES and constrains the non-longitudinal movement. Then, the movement is transmitted to two parallel-connected sub-CM named upper sub-CM and lower sub-CM. The upper sub-CM consists of two rotational hinges and two rigid rods, which are series connected to actuate the upper driving foot. Unlike the motion transmission of the upper sub-CM, there is an extra series-connected cellular hinge in the lower sub-CM, which reduces the stiffness of the lower-sub CM. Therefore, the stiffness of the two sub-CMs are different. The property of the asymmetric stiffness of the ASCM can cause a phase difference in displacement response between the upper and lower driving feet. The proposed SSPEA utilizes this phase difference to compensate for the backward motion. To make the effect of phase difference more obvious, a mass block was added after the cellular hinge. The proposed SSPEA weighs 227 g and is made of 45# steel (Chinese standard GB/T 699-2015), whose density, Young’s modulus and Poisson’s ratio are 7890 kg/m^3, 209 GPa and 0.27, respectively. The key dimensions are shown in Table 1. This SSPEA based on the ASCM is an improvement on the SSPEA based on the collaborative compensation CM (CCCM) proposed in [21]. The difference is that the compensation effect of the ASCM in this article is better after 250 Hz, while due to the issues of signal accuracy and mechanism delay, the compensation effect of the CCCM is better before 200 Hz. The reason for this phenomenon is that when the frequency exceeds 250 Hz, a sufficient phase difference is established between the upper and lower driving feet, thereby compensating for the backward motion. Moreover, two PESs are required in [21], while in this paper only one PES is needed.

2.2. Working principle

The working principle of the proposed actuator is presented in Fig. 3. A sawtooth signal (with asymmetry of 90%) is applied to the PES, causing the actuator to produce stick–slip motion. When the motion stabilizes, the work process within a cycle can be divided into the following four stages: initial stage, cooperation stage, compensation stage, and backward stage.

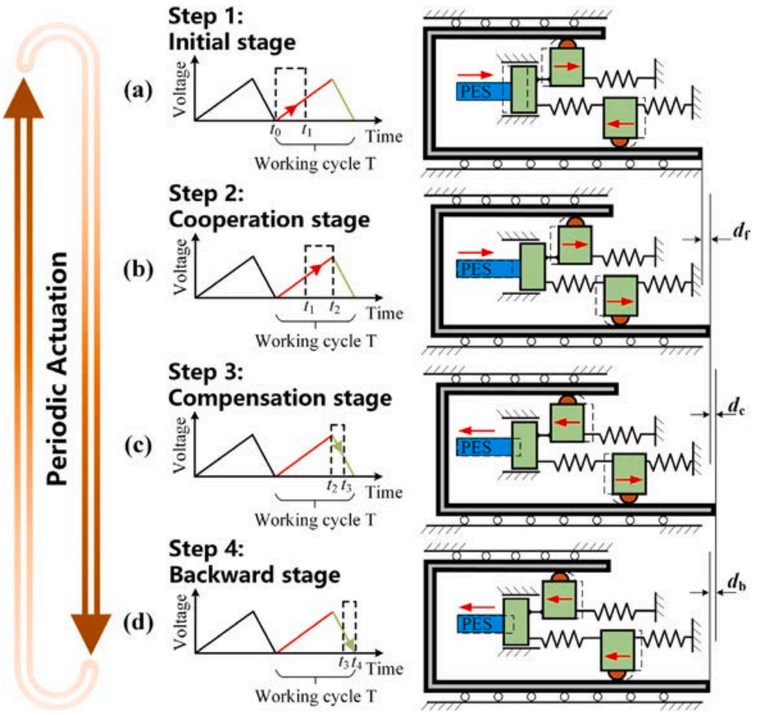

Fig. 3. Working principle of the proposed actuator with asymmetric stiffness compliant mechanism. (a) Step 1: initial stage. (b) Step 2: cooperation stage. (c) Step 3: compensation stage. (d) Step 4: backward stage.

Step 1 t_0-t_1 Initial stage: For any of the static working cycles, the PES moves forward after being energized. Due to the different stiffness of the upper and lower driving feet, the response of the upper driving foot is faster than that of the lower driving foot. Therefore, the upper driving foot starts to move forward first, and the lower driving foot is still maintaining a backward motion. So in this stage, the slide remains stationary.

Step 2 t_1-t_2 Cooperation stage: In this stage, the PES continues to elongate. The upper and lower driving feet move forward together, and the slider moves forward through static friction between the two driving feet and the slider. The forward displacement in this stage is denoted as d_f.

Step 3 t_2-t_3 Compensation stage: In this stage, the PES begins to contract. The upper driving foot begins to move backward at t_2. However, because of the slower response of the lower driving foot to the signal compared to the upper driving foot, the lower driving foot begins to move forward. Therefore, due to the comprehensive effect of the lower and upper driving foot, the slider continues to move forward for a short distance at this stage, which is denoted as d_c.

Step 4 t_3-t_4 Backward stage: In this stage, the PES keeps contracting and drives the upper and lower driving feet to move backward. Due to the backward dynamic friction, the slide moves backward, and the backward distance is marked as d_b. Because d_f+d_c is larger than d_b, the slider can move forward within each cycle. By repeating the above steps, the slider can achieve theoretically infinite working strokes step by step under the driving of the PES.

3. Modeling and simulation

3.1. Kinematic modeling

Assuming that: (1) The elastic deformation of the PEA only occurs at the flexure hinges and the other components are considered as rigid bodies. (2) The deformation of the flexure hinges is assumed to be pure bending and the rotational angle is small without any expansion and contraction deformations. According to the pseudo-rigid-body model approach, the equivalent model of the ASCM can be derived as presented in Fig. 4. The letter i ($i = A, B, \ldots, H$) denotes the rotational centers of the flexure hinges. d_in is the input displacement of the PEA. d_out1 and d_out2 are the output displacement of the two driving feet, respectively.

In the linkage mechanism, Φ_i (i =1, 2, …, 6) is the initial angular and l_i (i =1, 2, …, 6) are the lengths of the linkages. S_1 and S_2 are vectors attached to linkages AC and DH, respectively. α is the angle between linkages EF and FH. Based on geometric and

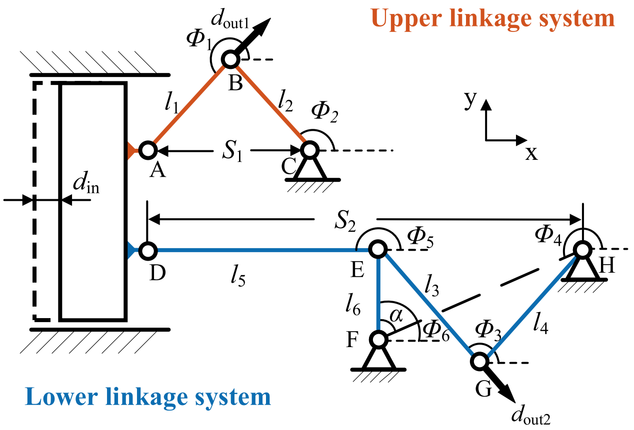

Fig. 4. Pseudo-rigid-body model of the proposed actuator.

kinematic relationships, the following equation can be obtained from the upper driving foot:

$$l_2 e^{i\Phi_2} + l_1 e^{i\Phi_1} = S_1 e^{i\pi}. \tag{1}$$

Differentiating Eq. (1) with respect to time yields

$$l_2\omega_2 e^{i\left(\Phi_2+\frac{\pi}{2}\right)} + l_1\omega_1 e^{i\left(\Phi_1+\frac{\pi}{2}\right)} = \dot{S}_1 e^{i\pi}, \tag{2}$$

where ω_1 and ω_2 represent the angular speed of linkages AB and BC, respectively. Let the real and imaginary parts be equal, and thus the following equation can be obtained:

$$\begin{cases} l_2\omega_2 \sin\Phi_2 + l_1\omega_1 \sin\Phi_1 = \dot{S}_1 \\ l_2\omega_2 \cos\Phi_2 + l_1\omega_1 \cos\Phi_1 = 0. \end{cases} \tag{3}$$

The displacement amplification ratio of the upper linkage system R_{amp1} can be represented as follows:

$$R_{\text{amp1}} = \frac{\partial d_{\text{out1}}}{\partial d_{\text{in}}} = \frac{\partial d_{\text{out1}}/\partial t}{\partial d_{\text{in}}/\partial t} = \frac{\cos\Phi_1}{\sin\Phi_2\cos\Phi_1 - \sin\Phi_1\cos\Phi_2}. \tag{4}$$

Similarly, the displacement amplification ratio of the lower linkage systems R_{amp2} can be represented as follows:

$$R_{\text{amp2}} = \frac{\partial d_{\text{out2}}}{\partial d_{\text{in}}} = \frac{\partial d_{\text{out1}}/\partial t}{\partial d_{\text{in}}/\partial t} = \frac{1}{\sin\Phi_4 + \frac{\sin\Phi_3\sin(\Phi_4-\Phi_6)}{\sin(\Phi_6-\Phi_3)} - \frac{\sin(\Phi_4-\Phi_6)\cos\Phi_3+\cos\Phi_4\sin(\Phi_6-\Phi_3)}{\cos\Phi_5\sin(\Phi_6-\Phi_3)}\sin\Phi_5}. \tag{5}$$

3.2. Static modeling

Based on the pseudo-rigid-body model method, a static model was established for the force–deflection relationship of the flexible hinges. By replacing the flexible hinges with equivalent rigid joints and torsion springs, the actuator would then be transformed into a rigid body mechanism. Therefore, traditional rigid body static analysis can be carried out to further study the performance of the actuator and obtain various key design parameters. To derive the input stiffness of CM, Castiglione's first theorem was adopted and expressed as

$$F_{\text{in}} = \frac{\partial U}{\partial d_{\text{in}}} \tag{6}$$

where F_{in} is the applied force, and U is the deformation energy and given as

$$U = \frac{1}{2}\sum_{i=\text{A}}^{\text{H}} K_{\text{r}i}{\psi_i}^2 + \frac{1}{2}K_{\text{fg}}{d_{\text{in}}}^2, i = \text{A, B, C, E, F, G, H} \tag{7}$$

where $K_{\text{r}i}$ (i=A, B, C, E, F, G, H) are the torsion spring constants of rotational hinges, K_{fg} is the torsion spring constant of flexure-guided hinge, ψ_i (i=A, B, C, E, F, G, H) are the angle increments of rotational flexure hinges.

When a small displacement d_{in} from PES is applied to the input end of the CM, the angle increment of the rotational flexure hinges ψ_i (i=A, B, C, E, F, G, H) can be calculated as follows:

$$\begin{cases} \psi_{\text{A}} = a\dfrac{d_{\text{in}}}{\varepsilon_1} \\ \psi_{\text{B}} = a\dfrac{d_{\text{in}}}{\varepsilon_1} - \dfrac{d_{\text{in}}}{\varepsilon_1} = \dfrac{(a-1)\, d_{\text{in}}}{\varepsilon_1} \\ \psi_{\text{C}} = \dfrac{d_{\text{in}}}{\varepsilon_1} \\ \psi_{\text{E}} = c\dfrac{d_{\text{in}}}{\varepsilon_2} - b\dfrac{d_{\text{in}}}{\varepsilon_2} = \dfrac{(c-b)\, d_{\text{in}}}{\varepsilon_2} \\ \psi_{\text{F}} = d\dfrac{d_{\text{in}}}{\varepsilon_2} \\ \psi_{\text{G}} = b\dfrac{d_{\text{in}}}{\varepsilon_2} - \dfrac{d_{\text{in}}}{\varepsilon_2} = \dfrac{(b-1)\, d_{\text{in}}}{\varepsilon_2} \\ \psi_{\text{H}} = \dfrac{d_{\text{in}}}{\varepsilon_2} \end{cases} \tag{8}$$

with

$$\begin{cases} a = \dfrac{\omega_1}{\omega_2} = -\dfrac{l_2 \cos \Phi_2}{l_1 \cos \Phi_1} \\ b = \dfrac{\omega_3}{\omega_4} = \dfrac{l_4 \sin\left(\Phi_4 - \Phi_6\right)}{l_3 \sin\left(\Phi_6 - \Phi_3\right)} \\ c = \dfrac{\omega_5}{\omega_4} = -\dfrac{l_4\left(\cos \Phi_4 \sin\left(\Phi_6 - \Phi_3\right) + \cos \Phi_3 \sin\left(\Phi_4 - \Phi_6\right)\right)}{l_5 \cos \Phi_5 \sin\left(\Phi_6 - \Phi_3\right)} \\ d = \dfrac{\omega_6}{\omega_4} = \dfrac{l_4 \sin\left(\Phi_3 - \Phi_4\right)}{l_6 \sin\left(\Phi_3 - \Phi_6\right)} \\ \varepsilon_1 = \dfrac{\dot{S}_1}{\omega_2} = a l_1 \sin \Phi_1 + l_2 \sin \Phi_2 \\ \varepsilon_2 = \dfrac{\dot{S}_2}{\omega_4} = b l_3 \sin \Phi_3 + l_4 \sin \Phi_4 + c l_5 \sin \Phi_5. \end{cases}$$

The angle increment of the rotational flexure hinges ψ_i are obtained based on the principle of differential approximation. An example is provided to facilitate a better understanding. To calculate the increased angle ψ_{A} of flexure hinge A, the derivation process is as follows. ε_1 represents the ratio of the velocity of the flexure-guided hinge $\dot{S}_1$ to the angular velocity ω_2 of linkage BC, while a represents the ratio of the angular velocity ω_1 of linkage AB to the angular velocity ω_2 of linkage BC. According to the principle of differential approximation, when the displacement is sufficiently small, the ratio of displacements is equal to the ratio of velocities, which leads to the first formula in Eq. (8).

According to the strength of materials, linear elasticity, and Saint Venant principle, the torsion spring constants of all hinges in ASCM can be obtained by

$$\begin{cases} K_{\text{r}i} = \dfrac{ETw_i^{\,3}}{12 l_i}, i = \text{A, B, C, E, F, G, H} \\ K_{\text{fg}} = \dfrac{4ETw_{\text{fg}}^{\,3}}{l_{\text{fg}}^{\,3}} \end{cases} \tag{9}$$

where E and T are Young's modulus and thickness of ASCM, respectively. l_i and l_{fg} represent length of the ith flexural hinge and the flexure-guided hinge, respectively. w_i and w_{fg} denote width of the ith flexural hinge and the flexure-guided hinge, respectively.

The input stiffness of the CM K_{in} can be derived as

$$K_{\text{in}} = \frac{F_{\text{in}}}{d_{\text{in}}} = \frac{a^2 K_{\text{rA}}}{{\varepsilon_1}^2} + \frac{(a-1)^2 K_{\text{rB}}}{{\varepsilon_1}^2} + \frac{K_{\text{rC}}}{{\varepsilon_1}^2} + \frac{(c-b)^2 K_{\text{rE}}}{{\varepsilon_2}^2} + \frac{d^2 K_{\text{rF}}}{{\varepsilon_2}^2} + \frac{(b-1)^2 K_{\text{rG}}}{{\varepsilon_2}^2} + \frac{K_{\text{rH}}}{{\varepsilon_2}^2} + K_{\text{fg}} \tag{10}$$

Similarly, the stiffness of the upper compliant mechanism K_{up} and the stiffness of the lower compliant mechanism K_{low} between can be obtained:

$$K_{\text{up}} = \frac{a^2 K_{\text{rA}}}{{\varepsilon_1}^2} + \frac{(a-1)^2 K_{\text{rB}}}{{\varepsilon_1}^2} + \frac{K_{\text{rC}}}{{\varepsilon_1}^2} + K_{\text{fg}} \tag{11}$$

$$K_{\text{low}} = \frac{(c-b)^2 K_{\text{rE}}}{{\varepsilon_2}^2} + \frac{d^2 K_{\text{rF}}}{{\varepsilon_2}^2} + \frac{(b-1)^2 K_{\text{rG}}}{{\varepsilon_2}^2} + \frac{K_{\text{rH}}}{{\varepsilon_2}^2} + K_{\text{fg}} \tag{12}$$

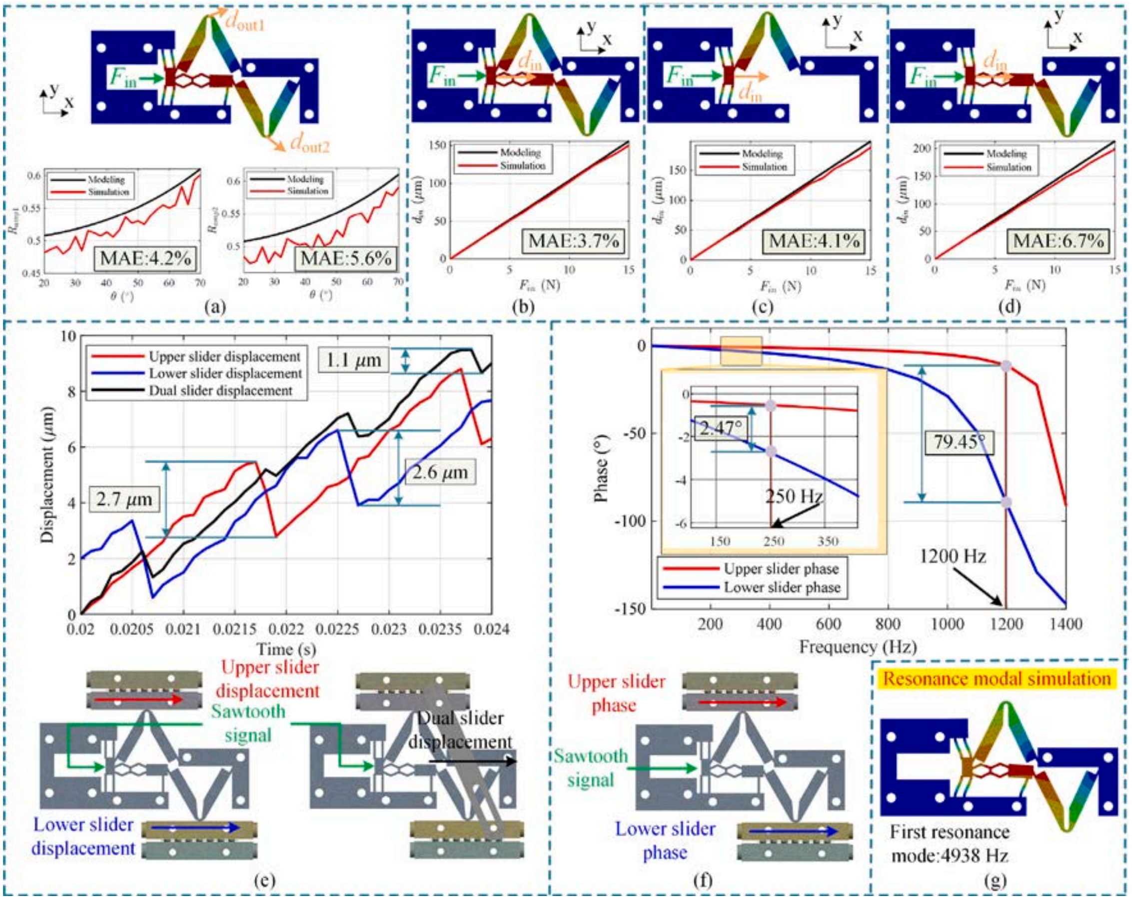

Fig. 5. Finite element analysis results of the designed compliant mechanism. (a) Finite element analysis of amplification ratio. (b) Finite element analysis of the stiffness of the designed compliant mechanism. (c) Finite element analysis of the stiffness of the upper compliant mechanism. (d) Finite element analysis of the stiffness of the lower compliant mechanism. (e) Finite element analysis of slider displacement. (f) Finite element analysis of slider phase. (g) Finite element analysis of resonance mode.

When two driving feet bear a load of force, the relationship between the input force F_{in} and the output displacement and force load of the two driving feet is:

$$F_{\text{in}} = K_{\text{in}} d_{\text{in}} + R_{\text{amp1}} F_{\text{out1}} + R_{\text{amp2}} F_{\text{out2}} \tag{13}$$

where F_{out1} and F_{out2} are the output force of the upper and lower driving feet, respectively.

When designing the ASCM, the goal is for it to withstand greater loads and deliver higher speeds, that is, to expect greater output force and greater amplification ratio. But these two goals are clearly contradictory to each other. In fact, assuming that the output force and displacement of PES are constants, there is an inverse relationship between the amplification ratio and output force. Therefore, it is necessary to optimize the parameters of ASCM in order to make a trade-off between the amplification ratio and output force.

3.3. Finite element simulation

In this part, FE simulation is conducted in the ANSYS software. On the one hand, the simulation results are used to validate the analytical models proposed above; and on the other hand, the results are used to determine the structural parameters of the physical prototype for the subsequent experimental tests. The input of the real PES is replaced by adding specified force or displacement inputs for different simulation purposes. 45# steel is selected as the material for the actuator. For more details on the material parameters, please refer to Section 2.1. The FE analysis results are presented in Fig. 5, and the derived structural parameters of the proposed ASCM are summarized in Table 1. The FE simulation processes are introduced as follows.

3.3.1. Static simulation

As shown in Fig. 5(a), to obtain the amplification ratio of the upper and lower linkage system, input displacement is set at the flexure-guided hinge. The output displacement of the upper and lower driving feet is obtained to calculate the amplification ratio of

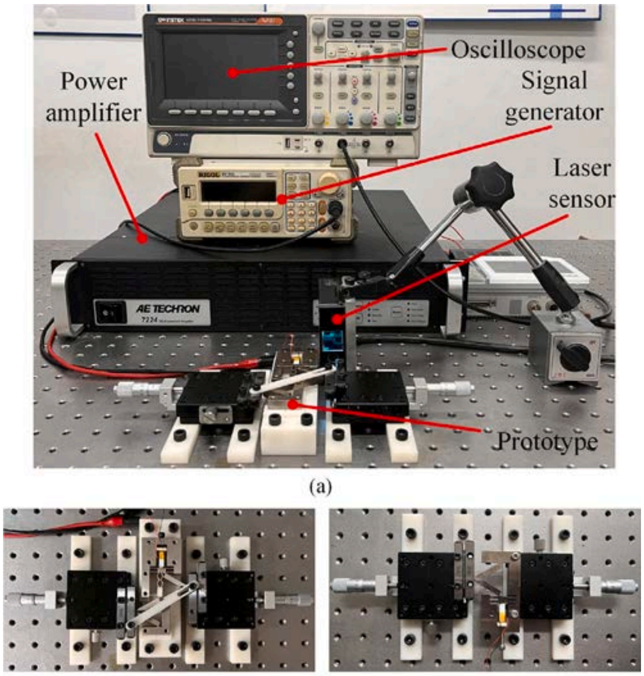

(a)

(b) (c)

Fig. 6. Experimental system. (a) Configuration of the test bench. (b) Enlarged view of the proposed asymmetric stiffness compliant mechanism. (c) The traditional triangular compliant mechanism for comparison.

the upper and lower linkage system. Assuming that the angle between linkage AB and BC is the same as the angle between linkage EG and GH, both are θ. According to the simulation results, the mean absolute error (MAE) between the analytical model and FE simulation for R_{amp1} and R_{amp2} are 4.2% and 5.6%, respectively, indicating the accuracy of the theoretical model. At the same time, it is concluded that as θ increases, the amplification ratio of the mechanism decreases.

As depicted in Fig. 5(b), (c), and (d), to determine the stiffness of the proposed CM, an input force is applied at the flexure-guided hinge. The output displacement of the flexure-guided hinge is then measured to calculate the stiffness. Based on the simulation results, two conclusions can be drawn. First, comparing the analytical modeling results of K_{in}, K_{up}, and K_{low} with the simulation results shows that the errors are 3.1%, 4.1%, and 3.7%, respectively. The errors between the simulation results and the analytical modeling results are all within 5%, indicating the accuracy of the analytical modeling. Second, there is a stiffness difference between the upper CM K_{up} and the lower CM K_{low}, which ensures that the ASCM can generate a phase difference during operation as designed, thereby compensating for return errors.

3.3.2. Dynamic simulation

As shown in Fig. 5(e), a 90% asymmetric sawtooth wave signal with a frequency of 600 Hz is set at the flexure-guided hinge. Observing the displacement of the slider, it can be seen that there is a significant phase difference between the upper and lower driving feet of the ASCM, caused by the asymmetric stiffness. Compared with single-foot driving, the return error of dual-foot driving has decreased from 2.6 μm to 1.1 μm, indicating that the proposed ASCM effectively suppresses the return error.

As shown in Fig. 5(f), by setting sawtooth wave signals with different frequencies at the flexure-guided hinge and observing the displacement of the upper and lower sliders, the relationship between the phase and frequency of the upper and lower sliders can be determined. According to the simulation results, when the frequency of the triangular wave is 250 Hz, a phase difference of 2.47° begins to appear between the upper and lower sliders. This corresponds to the experimental results. In the step length test, the step size of the ASCM starts to exceed that of the TTCM at 300 Hz. Moreover, the phase difference between the upper and lower sliders increases with the frequency, reaching a maximum of 79.45° at 1200 Hz.

As shown in Fig. 5(g), FE modal simulation was conducted on the proposed actuator, revealing that the first resonance mode of the actuator is 4938 Hz.

4. Experimental tests

4.1. Experimental setup

To measure the output performance of the proposed prototype, an experimental system was established, as shown in Fig. 6. A 5 mm × 5 mm × 18 mm PES (NAC2013-H18, Core Tomorrow Co., Ltd., China) is chosen as the power source to actuate the ASCM.

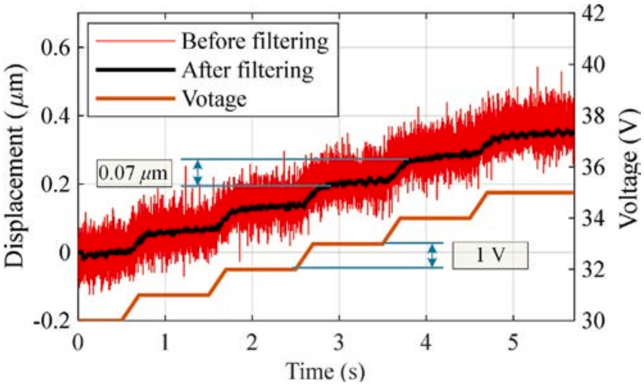

Fig. 7. Resolution test of the proposed actuator.

Two sliders (CGDV-H18-L50, SAMLO Co., Ltd., China) are fixed on two micro-adjusting platforms (CGZX60, SAMLO Co., Ltd., China) for adjusting the pre-load. The configuration of the test bench is shown in Fig. 6(a). The input sawtooth waveform voltage signal is generated by the signal generator (DG1022, ROGOL Co., Ltd., China), and is displayed and recorded through an oscilloscope (GDS-1104B, Taiwan Cuswell Electronics Co., Ltd., China). Then, it is amplified by a power amplifier (7224, AE Techron Inc., USA) for voltage amplification. The horizontal movement of the slider is measured by a laser displacement sensor (CD5-30A, GOCATOR Co., Ltd., China), and the data is transmitted to the oscilloscope for display and recording.

Fig. 6(b) presents the enlarged view of the proposed actuator with ASCM. To demonstrate the superiority of the proposed actuator, comparative experiments were conducted using a traditional triangular CM (TTCM) under the same experimental conditions. The experimental prototype of the TTCM is shown in Fig. 6(c).

4.2. Resolution test

Resolution is an important index for actuators for its wide usage in precision driving situations so it is an important performance indicator of SSPEAs. The resolution of the prototype is measured by providing a stepped voltage driving signal to the PES. The experimental results are shown in Fig. 7. To clearly present the sensor results, a Butterworth low-pass filter was used. The filter is of third order with a cutoff frequency of 1000 Hz. The voltage between adjacent steps is 1 V, and the resolution of the actuator is 0.07 μm. In fact, when the voltage difference between adjacent steps is smaller, the actuator can achieve a finer resolution. However, due to the measurement accuracy limitations of the sensor, the actuator's resolution is only measurable down to 0.07 μm.

4.3. Step size test

For PEAs, step size is an important optimization parameter. In the following experiment, the relationship between step size and driving signal frequency was studied. The output speed and step size of ASCM and TTCM at different frequencies were compared under 75 V driving voltage to demonstrate the effect of asymmetric stiffness method compensation. The driving voltage of 75 V was chosen for convenience in comparison with the work done by Qiu et al. [21]. The experimental results are shown in Fig. 8. Between 50 Hz and 1200 Hz, as the driving frequency increases, the step size of ASCM increases from 1.34 μm to 11.63 μm. Assuming that the ratio of step size between ASCM and TTCM is defined as κ. The ratio κ has a significant increase from 250 Hz, reaching a maximum value of 2.51 at a driving frequency of 1200 Hz. This is because, when the driving frequency reaches 250 Hz, the phase difference between the upper and lower driving feet becomes significant enough to compensate for the backward motion. When the frequency exceeds 1200 Hz, an increase in frequency leads to a decrease in step size. This can be understood because excessive driving foot speed can affect the original stick–slip motion. Remarkably, at a driving frequency below 400 Hz, the output displacement results of the slide obtained using TTCM are consistent with those obtained by Qiu et al. [21].

4.4. Speed test

4.4.1. Speed test under different driving voltages

Firstly, the relationship between the output speed of the slider and the driving voltage was studied. The driving signal frequency was kept constant at 600 Hz, and the driving voltages were selected as 40 V, 60 V, 80 V, and 100 V, respectively. Experimental tests were conducted on the no-load output speeds of ASCM and TTCM. As shown in Fig. 9(a), at a driving frequency of 600 Hz, even with voltage changes, the no-load speed of ASCM is higher than the value of TTCM. When the driving voltage is 40 V, the no-load speed of ASCM is 1.77 mm/s, which is 1.72 times that of TTCM. When the driving voltage increases to 100 V, the no-load speed of ASCM increases to 6.42 mm/s, which is 1.21 times that of TTCM. The advantage of speed would be more apparent as the driving frequency increases. Because as the driving frequency increases, the phase difference between the two driving feet will be more

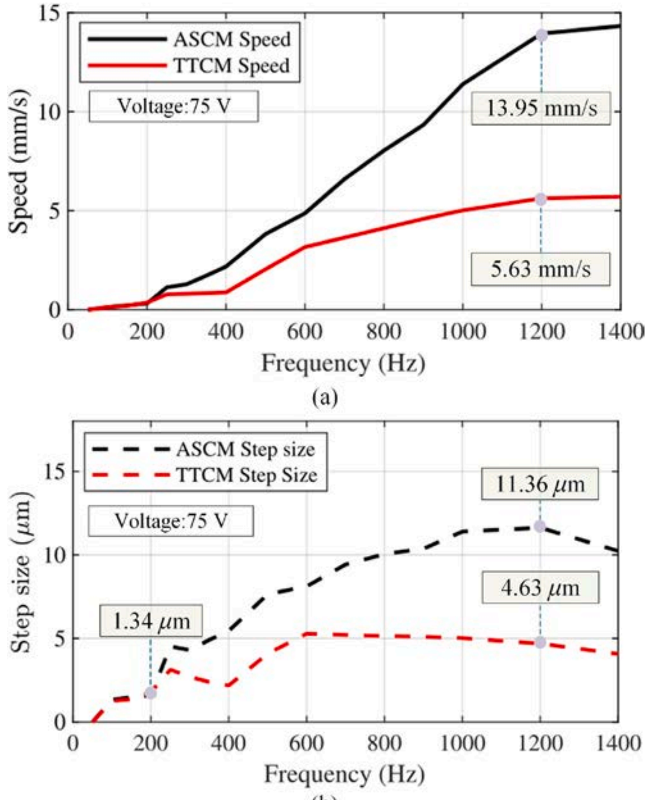

(a)

(b)

Fig. 8. Step size test. (a) Speed test at different frequencies when the driving voltage is 75 V. (b) Step size test at different frequencies when the driving voltage is 75 V.

significant, and the compensation effect will also be better. When the driving frequency is higher than 250 Hz, the no-load speed of ASCM is already higher than that of TTCM. It is worth mentioning that under different driving voltages, the time–displacement output curve of the actuator still exhibits good linearity. After calculation, all the linear fit r_2 of the displacement curves under different voltages are all above 0.99. This indicates that the output characteristics of the actuator are very stable.

4.4.2. Speed test under different driving frequencies

In addition, Fig. 9(b) shows the relationship between the output speed and frequency of the slide. Firstly, it is necessary to determine the optimal driving frequency of the driver. However, due to the limitation of the output power of the PES, it is necessary to appropriately reduce the driving voltage when the driving frequency is high. Thus when conducting the optimal frequency experiment for the driver, the driving voltage is selected as 40 V. In addition, FE analysis was used to simulate the output speed of the ASCM under a 40 V driving voltage, and the results were compared with experimental results. It can be seen that the optimal driving frequency obtained from the FE simulation results is very close to the optimal driving frequency measured from the experimental results. The simulation result is 2600 Hz, and the experimental result is 2400 Hz. The modal simulation of the actuator in Section 3.3.2 shows that the first resonance mode of the actuator is at 4938 Hz. The main frequency components of the 2400 Hz triangular signal (90% asymmetry) are 2400 Hz and 4800 Hz. As a result, the 4800 Hz frequency component of the triangular signal excites the first resonance mode of the actuator, causing a sharp increase in output speed. This indicates that the mechanism has entered resonance, and operation at this frequency should be avoided. Due to the presence of damping in actual mechanical structures, it is difficult to test in experiments. Therefore, after reviewing the relevant papers on piezoelectric actuators, the damping ratio in the finite element simulation was set to 0.05 based on [29]. This is an approximate value that may result in the optimal driving frequency obtained from the simulation results being lower than the experimental results. At the same time, the output speed of the simulated slide is greater than the experimental results, because the simulation did not take into account the energy loss of the hinge, PES, driving foot, and other positions during the experimental process.

4.5. Load test

In practical applications, PEAs need to carry a certain load. A load experiment was designed using pulleys and weights, and the experimental results are shown in Fig. 10. Due to the limitation of the output power of the piezoelectric stack, the values of

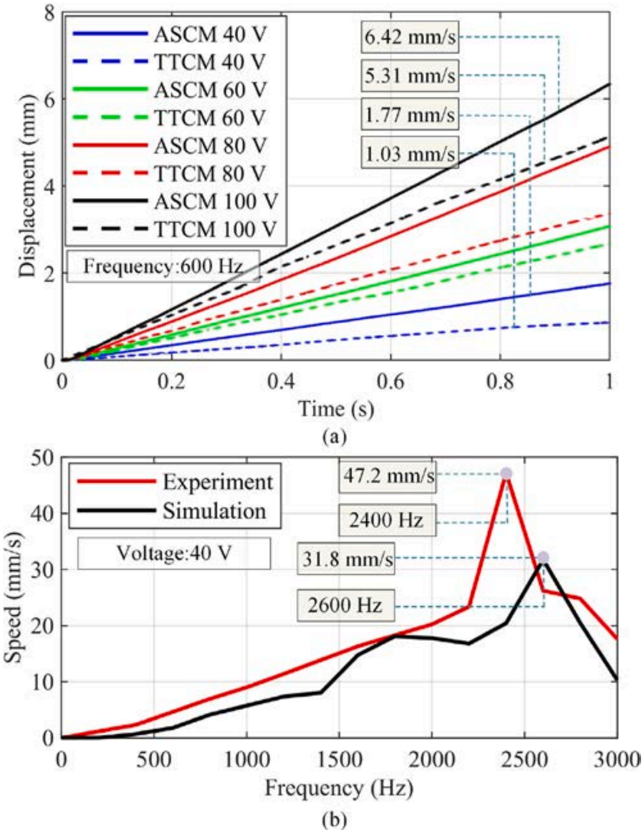

Fig. 9. Speed test. (a) Speed test at different voltages when the driving frequency is 600 Hz. (b) Speed test at different frequencies when the driving voltage is 40 V.

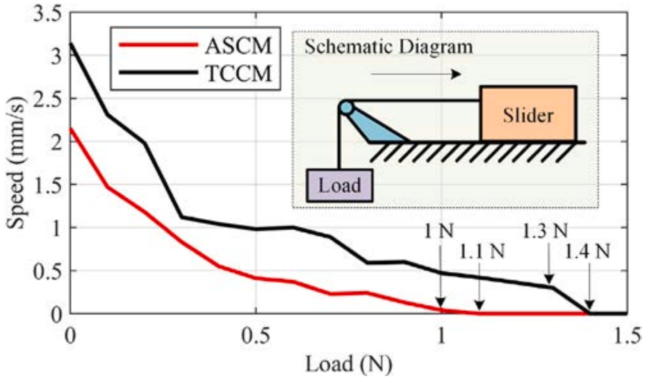

Fig. 10. Relationship between the load and the slider output speed at 600 Hz and 60 V.

the voltage and frequency of the driving signal cannot be large at the same time. So a compromise approach was adopted in the load experiment, with a driving frequency of 600 Hz and a driving voltage of 60 V. The experimental results indicate that as the horizontal load increases, the output speed of the slider will also decrease. When the horizontal load reaches 1.3 N, the output speed of the ASCM slider decreases to 0.3 mm/s. From this, it can be seen that the horizontal load capacity of the proposed actuator is 1.3 N. However, when the horizontal load is 1 N, the TTCM slider output has decreased to 0.04 mm/s, and its horizontal load capacity is 1 N. Of note, after applying a horizontal load, the time–displacement output curve of the actuator still exhibits good linearity. After calculation, all the linear fit r_2 of the experimental results under different loads are all above 0.99. This indicates that the output characteristics of the actuator are relatively stable after applying a horizontal load.

Table 2
Summary of remarkable research of active needles with key features.

Parameter	Driving signal	Multi-drive-mode PEA [30]	Snake-inspired PEA [31]	TTCM [18]	CCCM [21]	ASCM (This work)
No-load speed (mm/s)	75 V, 400 Hz	0.92 (50 V, 450 Hz)	1.85 (100 V, 400 Hz)	0.88	1.4	2.18
Step size (μm)	75 V, 400 Hz	2.04 (50 V, 450 Hz)	4.63 (100 V, 400 Hz)	2.19	3.51	5.45
Step amplification ratio	75 V, 400 Hz	/	/	/	1.60	2.49
Horizontal load capacity (N)	60 V, 600 Hz	3 (75 V, 500 Hz)	2.8 (100 V, 600 Hz)	1	/	1.3
Compliant mechanism size (mm)	/	$70 \times 59 \times 12$	$70 \times 59 \times 30$	$100 \times 50 \times 42$	/	$97 \times 88 \times 21$
PES (mm)	/	$5 \times 5 \times 10$ (double)	$5 \times 5 \times 20$	$5 \times 5 \times 18$	$5 \times 5 \times 18$ (double)	$5 \times 5 \times 18$

5. Discussions

5.1. Output speed

Table 2 highlights the superior performance of the proposed SSPEA based on various output metrics. The output speed of the slider under no-load conditions was compared across different mechanisms. When the driving frequency exceeds 250 Hz, the no-load output speed of the slider in the PEA proposed in this paper surpasses that of the TTCM. This advantage becomes more pronounced as the driving frequency increases. The underlying reason is that higher driving frequencies result in a more significant phase difference between the two driving feet, leading to enhanced compensation effects.

5.2. Maximum step

The maximum step displacement of different mechanisms under no-load conditions was compared. When the driving frequency is below 200 Hz, CCCM exhibits a superior compensation effect. Specifically, at a driving frequency of 10 Hz, the step size of the CCCM can reach up to 29 times that of the TTCM [18]. However, as the driving frequency increases, the compensation effect of CCCM diminishes gradually. When the frequency exceeds 350 Hz, the compensation effect of the ASCM PEA proposed in this paper becomes more effective than that of the CCCM. Particularly, at a driving frequency of 1200 Hz, the step size of the ASCM can achieve 11.6 μm.

5.3. Load capacity

In terms of horizontal load capacity, the ASCM can carry a load of 1.3 N, whereas the TTCM can only support a load of 1 N. This further underscores the enhanced performance and robustness of the ASCM mechanism compared to the TTCM under various operational conditions.

6. Conclusion

In summary, a new type of SSPEA based on the principle of asymmetric stiffness is proposed. In order to generate asymmetric stiffness between the input end and the upper and lower driving feet, an ASCM was designed. This mechanism has two driving feet, upper and lower, and a honeycomb-shaped spring is designed between the lower driving foot and the input end. The stiffness difference between the upper and lower driving feet creates a phase difference, thereby compensating for the backward motion of the stick–slip motion. According to theoretical calculations, the amplification ratio between the two driving feet and the input end is 0.577, the overall stiffness is 14.42 N/μm, the stiffness of the upper half is 13.24 N/μm, and the stiffness of the lower half is 14.24 N/μm. The theoretical calculation results were validated using FE analysis, and the error of the results was within 7%. In order to verify the feasibility of the proposed driver, a prototype was made for testing. The experimental results indicate that when the driving frequency is greater than 250 Hz, the asymmetric compensation of the ASCM mechanism begins to have an effect. When the driving frequency is between 250 Hz and 1200 Hz, the higher the frequency, the better the compensation effect. Its step shift can reach 2.5 times that of TTCM at a driving frequency of 1200 Hz. Moreover, the proposed ASCM has a horizontal load capacity of 1.4 N, which is also superior to the load capacity of TTCM (1 N).

Compared with CCCM, the proposed in this paper is more suitable for compensating for backward motion in the high-frequency range. This work provides an effective method to improve the speed and load capacity of the stick–slip piezoelectric motor without increasing the PES and improves the comprehensive performance of the stick–slip piezoelectric driver. Future work will focus on theoretical modeling, friction modeling, piezoelectric hysteresis control in scanning mode, and practical applications of triangular CMs.

CRediT authorship contribution statement

Jie Ling: Writing – original draft, Investigation, Funding acquisition. **Hongtao Peng:** Validation, Data curation. **Yuzhou Duan:** Validation, Investigation. **Micky Rakotondrabe:** Writing – review & editing, Supervision, Conceptualization.

Declaration of competing interest

The authors declare that they have no known competing financial interests or personal relationships that could have appeared to influence the work reported in this paper.

Data availability

No data was used for the research described in the article.

References

[1] M. Xun, H. Yu, Y. Liu, J. Deng, S. Zhang, K. Li, A precise rotary piezoelectric actuator based on the spatial screw compliant mechanism, IEEE/ASME Trans. Mechatronics 28 (1) (2022) 223–232.

[2] Z. Zhang, P. Yan, Infinite dimensional design approach of robust disturbance observer for a piezo-actuated nano-positioner with measurement delays, IEEE/ASME Trans. Mechatronics 28 (6) (2023) 3583–3588.

[3] Y. Duan, H. Peng, Y. Zhu, Y. Shen, J. Ling, Inertial piezoelectric actuation of a needle insertion device for minimally invasive surgery, in: 2023 IEEE International Conference on Robotics and Biomimetics, ROBIO, 2023, pp. 1–6.

[4] Y. Duan, J. Ling, Y. Zhu, Modeling and admittance control of a piezoactuated needle insertion device for safe puncture of spinal membranes, J. Med. Dev. 18 (3) (2024) 034501.

[5] Y. Zhang, J. Ling, Y. Zhu, Development and fault-tolerant control of a distributed piezoelectric stack actuator, Smart Mater. Struct. (2024) http://dx.doi.org/10.1088/1361-665X/ad669e.

[6] J. Ling, M. Rakotondrabe, Z. Feng, M. Ming, X. Xiao, A robust resonant controller for high-speed scanning of nanopositioners: design and implementation, IEEE Trans. Control Syst. Technol. 28 (3) (2019) 1116–1123.

[7] M. Ling, X. He, M. Wu, L. Cao, Dynamic design of a novel high-speed piezoelectric flow control valve based on compliant mechanism, IEEE/ASME Trans. Mechatronics 27 (6) (2022) 4942–4950.

[8] Z. Lyu, Q. Xu, Novel design of a piezoelectrically actuated compliant microgripper with high area-usage efficiency, Precis. Eng. 76 (2022) 1–11.

[9] Y. Wang, J. Deng, H. Li, X. Tian, W. Chen, Y. Liu, A resonant-type thin plate piezoelectric actuator inspired by Koala's locomotion, IEEE Trans. Ind. Electron. 70 (8) (2023) 8235–8243.

[10] L. Wang, W. Chen, J. Liu, J. Deng, Y. Liu, A review of recent studies on non-resonant piezoelectric actuators, Mech. Syst. Signal Process. 133 (2019) 106254.

[11] J. Zhao, G. Mu, H. Dong, T. Sun, K.T.V. Grattan, Study of the velocity and direction of piezoelectric robot driven by traveling waves, IEEE Trans. Ind. Electron. 70 (9) (2022) 9260–9269.

[12] R. Wang, L. Wang, B. Jia, J. Jin, D. Wu, Semi-analytical modeling and experimental evaluation on a novel standing wave rotary piezoelectric actuator driven by single-phase signal, Mech. Syst. Signal Process. 163 (2022) 108177.

[13] W. Wang, J. Deng, J. Li, S. Zhang, Y. Liu, A small and agile ring-shaped tripodal piezoelectric robot driven by standing and traveling mechanical waves, IEEE Trans. Ind. Electron. 71 (3) (2024) 2769–2778.

[14] T. Sun, P. Yan, A novel high-speed bi-directional piezoelectric inchworm actuator based on flexible supported baffles, Smart Mater. Struct. 31 (9) (2022) 095014.

[15] J. Ling, L. Chen, Z. Feng, Y. Zhu, Development and test of a high speed pusher-type inchworm piezoelectric actuator with asymmetric driving and clamping configuration, Mech. Mach. Theory 176 (2022) 104997.

[16] W. Sun, Z. Xu, K. Wang, X. Li, J. Tang, Z. Yang, H. Huang, An impact inertial piezoelectric actuator designed by means of the asymmetric friction, IEEE Trans. Ind. Electron. 70 (1) (2022) 699–708.

[17] H. Huang, Y. Liu, Z. Xu, X. Li, W. Sun, H. Wu, Design, analysis and experimental performances of a multi-mode friction inertial piezoelectric actuator, Precis. Eng. 80 (2023) 180–197.

[18] Y. Zhang, Y. Peng, Z. Sun, H. Yu, A novel stick-slip piezoelectric actuator based on a triangular compliant driving mechanism, IEEE Trans. Ind. Electron. 66 (7) (2018) 5374–5382.

[19] P. Ning, X. Xia, G. Qiao, S. Yang, W. Ruan, X. Lu, R. Zheng, T. Cheng, A dual-mode excitation method of flexure hinge type piezoelectric stick-slip actuator for suppressing backward motion, Sensors Actuators A 330 (2021) 112853.

[20] J. Wang, H. Huang, H. Zhao, Model-based optimization for structure dimension and driving signal of a stick-slip piezoelectric actuator, Mech. Syst. Signal Process. 164 (2022) 108191.

[21] C. Qiu, J. Ling, Y. Zhang, M. Ming, Z. Feng, X. Xiao, A novel cooperative compensation method to compensate for return stroke of stick-slip piezoelectric actuators, Mech. Mach. Theory 159 (2021) 104254.

[22] J. Tang, H. Fan, J. Liu, H. Huang, Suppressing the backward motion of a stick-slip piezoelectric actuator by means of the sequential control method (SCM), Mech. Syst. Signal Process. 143 (2020) 106855.

[23] J. Dong, B. Zhang, X. Li, Z. Xu, J. Wang, C. Liu, Y. Cao, A stick-slip piezoelectric actuator with suppressed backward motion achieved using an active locking mechanism (ALM), Smart Mater. Struct. 30 (9) (2021) 095015.

[24] X. Tian, W. Chen, B. Zhang, Y. Liu, Restraining the backward motion of a piezoelectric stick-slip actuator with a passive damping foot, IEEE Trans. Ind. Electron. 69 (10) (2021) 10396–10406.

[25] Y. Liu, Z. Xu, X. Li, W. Sun, H. Huang, A high-performance stick-slip piezoelectric actuator achieved by using the double-stator cooperative motion mode (DCMM), Mech. Syst. Signal Process. 172 (2022) 108999.

[26] G. Qiao, H. Li, X. Lu, J. Wen, T. Cheng, Piezoelectric stick-slip actuators with flexure hinge mechanisms: A review, J. Intell. Mater. Syst. Struct. 33 (15) (2022) 1879–1901.

[27] S. Mohith, A.R. Upadhya, K.P. Navin, S. Kulkarni, M. Rao, Recent trends in piezoelectric actuators for precision motion and their applications: A review, Smart Mater. Struct. 30 (1) (2020) 013002.

[28] G. Qiao, P. Ning, X. Xia, Y. Yu, X. Lu, T. Cheng, Achieving smooth motion for piezoelectric stick-slip actuator with the inertial block structure, IEEE Trans. Ind. Electron. 69 (4) (2022) 3948–3958.

[29] J. Becker, O. Fein, M. Maess, L. Gaul, Finite element-based analysis of shunted piezoelectric structures for vibration damping, Comput. Struct. 84 (31–32) (2006) 2340–2350.

[30] H. Yun, D. Kong, M. Aoyagi, Development of a multi-drive-mode piezoelectric linear actuator with parallel-arrangement dual stator, Precis. Eng. 77 (2022) 127–140.

[31] L. Wang, H. Wang, Y. Zhang, Z. Qiu, T. Cheng, Development of a piezoelectric actuator based on stick-slip principle inspired by the predation of snake, Rev. Sci. Instrum. 94 (2) (2023) 025003.